Progress in Additive Manufacturing (2025) 10:9337–9353
https://doi.org/10.1007/s40964-025-01165-7

RESEARCH

Homogenization and artificial neural network prediction of elastic properties in triply periodic minimal surface structures

Mattia Mele[1] · Gianmarco Milan[1] · Andrea Paffetti[1] · Massimiliano De Agostinis[1] · Stefano Fini[1] · Giorgio Olmi[1] · Dario Croccolo[1]

Received: 3 March 2025 / Accepted: 7 May 2025 / Published online: 23 May 2025

Abstract

This study introduces a comprehensive framework for the generation, homogenization, and prediction of linear elastic properties of Triply Periodic Minimal Surface (TPMS)-based unit cells. Hybrid cells are created by combining four fundamental TPMS structures, namely primitive, gyroid, diamond, and I-WP. Finite element analysis is used to calculate the equivalent elastic properties of these structures. A dataset is generated using a full-factorial design of the experiment approach to train an Artificial Neural Network (ANN) for predicting the coefficients of the equivalent stiffness matrix. Findings demonstrate that the network can provide an accurate estimation of the elastic properties, thus significantly improving the efficiency of the design process. Particularly, the performances of the ANN overcome those of the Gibson-Ashby model in the orthotropic modeling of the cell. More importantly, the ANN is able to capture the anisotropy that arises by mixing the fundamental equations, thus allowing for an accurate representation of the actual behavior of the structure. This work contributes to the advancement of high-performance, lightweight materials, providing a robust and efficient methodology for the design of new structures to be produced via additive manufacturing.

Keywords Triply periodic minimal surface (TPMS) · Homogenization · Artificial neural network (ANN) · Design of experiment (DOE)

Abbreviations

AI	Artificial intelligence
AdaM	Adaptive moment estimation
AM	Additive manufacturing
ANN	Artificial neural network
API	Application programming interface
BCC	Body-centered cubic
BPNN	Back-propagation neural network
CNN	Convolutional neural network
DL	Deep learning
DLP	Digital light processing
DOE	Design of experiment
DoF	Degrees of freedom
FCC	Face-centered cubic
FDM	Fused deposition modeling
FEA	Finite element analysis
FF	Full factorial
FFF	Fused filament fabrication
GAM	Gibson-ashby model
IPC	Interpenetrating phase composite
L-PBF	Laser powder bed fusion
ML	Machine learning
ReLU	Rectified linear unit
RVE	Representative volume element
PBC	Periodic boundary conditions
SEA	Specific energy bbsorption
SHB	Shell-based

✉ Mattia Mele
mattia.mele@unibo.it

✉ Gianmarco Milan
gianmarco.milan@unibo.it

Andrea Paffetti
andrea.paffetti3@unibo.it

Massimiliano De Agostinis
m.deagostinis@unibo.it

Stefano Fini
stefano.fini@unibo.it

Giorgio Olmi
giorgio.olmi@unibo.it

Dario Croccolo
dario.croccolo@unibo.it

[1] University of Bologna, Bologna, Italy

SKB	Skeletal-based
SMM	Shell-based mechanical metamaterial
SLM	Selective laser melting
SLA	Stereolithography
TPMS	Triply periodic minimal surface
VF	Volume fraction

1 Introduction

Triply Periodic Minimal Surface (TPMS) structures represent a distinct class of cellular structures that, due to their unique geometric properties, offer promising applications across various engineering fields, including aerospace [1], automotive [2] and biomedical engineering [3]. These structures are characterized by a continuous surface with minimal mean curvature, providing a compelling combination of high specific strength, low density, and superior mechanical performance [4]. A recent survey by Gado et al. [5] highlighted that most studies discuss the use of TPMS structures in the fields of advanced architectured materials, lightweight structures, transportation, defense, and biomedical applications, with a recent surge in thermal management and water treatment. Due to their manufacturing complexity, the practical implementation of such structures has become feasible only with the development of Additive Manufacturing (AM) [6–8].

Unlike traditional lattice structures, such as strut-based or honeycomb geometries, TPMS have demonstrated significant mechanical and functional advantages, particularly for applications that require high energy absorption, specific stiffness, and tailored properties. These structures can be generated using implicit definitions based on specific level sets. Among the various configurations, this study focuses on shell-based (or sheet-based) TPMS structures, created by defining a solid volume enclosed between two isosurfaces symmetrically offset from a base surface. In contrast, skeletal-based (or solid-based) structures result from applying a level set to only one side of the base surface [9].

For example, Teng et al. [10] demonstrated that TPMS designs, particularly sheet-based Gyroid, outperform Body-Centered Cubic (BCC) lattices in energy absorption and compression stability due to their structural continuity. Similarly, Zhang et al. [11] showed that sheet-based Diamond TPMS structures provide stable collapse and high energy absorption under compression, along with superior stiffness. Al-Ketan et al. [12] further noted that TPMS shell-based structures, particularly Diamond and Gyroid, significantly outperform both skeletal-based TPMS and truss-based lattices, owing to their nearly stretching-dominated deformation modes.

In engineering design, TPMS topologies such as the Primitive, Gyroid, Diamond, and I-WP structures have been studied extensively for their fascinating mechanical properties, such as the elevated Specific Energy Absorption (SEA). For example, Abueidda et al. [13] presented a comparison between the mechanical properties of popular shell-based TPMS, namely Gyroid, I-WP, Neovius, and Primitive structures. Similarly, Feng et al. [14] focused on isotropy control within sheet-based TPMS designs for the four aforementioned topologies, while Callens et al. [15] specifically studied the shell-based Primitive and Gyroid structures using hyperbolic tiling theory to enable independent tuning of permeability and elastic properties. Daynes [16] also presented design strategies for achieving isotropy in sheet-based TPMS-based cellular structures, employing novel arrangements and optimization techniques to enhance energy absorption capabilities. Moreover, Yin et al. [17] investigated the crashworthiness of four TPMS sheet-based topologies (Primitive, F-RD, I-WP, and Gyroid). The authors also delved into how key geometrical parameters influence their mechanical performance, specifically the level constant in the implicit formulation of the TPMS geometry and the shell thickness of the TPMS sheets. However, the prediction and optimization of these properties in diverse applications remain challenging due to the intricate relationship between the TPMS geometry and the resultant mechanical behavior.

Due to the relevance of these structures, a considerable amount of research has focused on their optimization in the last years. Almesmari et al. [18] examined recent developments in the optimization of the design of TPMS structures, emphasizing the opportunity to tune different mechanical properties. Recent works have highlighted the possibility to model hybrid TPMS structures, combining existing topologies to generate novel geometries or suitably varying a TPMS topology to another one. AlQayidi et al. [19] investigated the hybridization of shell-based TPMS structures, highlighting the improvements in mechanical performance that can be achieved by combining different topologies. Moreover, Bonatti and Mohr [20] further investigated shell-lattice metamaterials that approximate TPMS topologies such as I-WP and Gyroid using a smooth shell approach.

Generation and optimization of TPMS structures involve several steps, beginning with the implicit definition of the fundamental TPMS geometry. Numerous studies have investigated the hybridization of TPMS topologies to enhance their mechanical properties. For example, Gao et al. [21] explored the multilevel mechanism of hybrid biomimetic sheet-based TPMS structures to achieve a balanced set of mechanical properties. Similarly, Zhang et al. [22] developed a multidimensional hybrid design for shell-based TPMS structures, demonstrating significant improvements in SEA under various loading conditions. Researchers such as Plocher and Panesar [23] proposed an alternative approach, examining the impact of density and unit cell size grading on the mechanical properties of functionally graded sheet-based

TPMS structures. Another pertinent study is provided by Ozdemir et al. [24], who analyzed blended shell-based structures utilizing appropriate merging functions. Their research integrated genetic algorithms for morphology selection and anisotropic homogenization-based topology optimization for grading designs. They fabricated cobalt-chromium structures with laser sintering and validated their enhanced mechanical efficiency through experimental tests, demonstrating significant improvements in stiffness over single lattice morphologies.

All these studies rely on well-established TPMS structures, while the design methodology depends on the spatial variation of cell size, geometry, or thickness. In contrast, this work focuses on the generation of new TPMS-based geometries, utilizing a weighted combination of known structures. This approach was previously adopted in some recently published works for the inverse design of TPMS-like structures targeting specific mechanical properties. Particularly, Chen et al. [25] used hybridization to design quasi-isotropic and ultra-stiff sheet-based structures. Patel et al. [26] constructed TPMS-based Interpenetrating Phase Composite (IPC) architectures using skeletal-based TPMS cells, while Wang et al. [27] and Hu et al. dealt with in their research [28] used homogenization for creating targeted Shell-based Mechanical Metamaterial (SMM). Recent research by Chen et al. [29] developed a computationally efficient approach employing Fast Fourier Transform (FFT)-based homogenization to accurately characterize effective elastic properties of sheet-based TPMS-based structures composed of self-repeated representative volume elements. In their work, hybridization of TPMS topologies was achieved by intersecting or combining distinct unit cells. On the other hand, the present study proposes a parametric method for systematically blending multiple fundamental TPMS geometries. Such an approach can tremendously expand the accessible design space, enabling tailored anisotropic behavior through finely controlled geometry variations and fostering the generation of spatially varying programmable materials with continuous transitions.

These studies rely on the forward extraction of mechanical properties through either numerical methods or experiments. In particular, Finite Element Analysis (FEA) require suitable processes to extract effective properties of complex structures, such as homogenization. Multi-scale homogenization techniques have been extensively explored. For example, Pais et al. [30] discussed advanced homogenization methods, demonstrating their effectiveness in predicting the mechanical behavior of sheet-based TPMS structures under various loading conditions. Gao et al. [31] introduced a topological shape optimization method using an energy-based homogenization approach to design 3D microstructured materials, while Somnic and Jo [32] provided a comprehensive review of homogenization methods for lattice materials. Furthermore, FEA homogenization has been experimentally validated by studies such as that of Zhmaylo et al. [33], who combined FEA with experimental validation to ensure the precision of their homogenization model.

When exploring a large design space, such as in the case of hybridization, inferring the mechanical properties of novel structures based on a finite number of simulations becomes a crucial goal. In this direction, Machine Learning (ML) and Artificial Intelligence (AI) models have been demonstrated to be powerful tools. Yang et al. [34] implemented a Deep Learning (DL) model to predict complete strain and stress tensors for composite materials, demonstrating high accuracy across complex microstructures, while Chen et al. [35] leveraged a Neural Network model to predict surface elastic properties in Face-Centered Cubic (FCC) metals. Furthermore, Li et al. [36] utilized image-based modeling combined with DL to predict effective moduli of heterogeneous materials, while Yu et al. [37] developed a DL-based strategy to design heterogeneous lattice structures with customized mechanical responses. Liu et al. [38] introduced a high-resolution topology optimization framework for multi-morphology lattice structures, integrating 3D Convolutional Neural Network (CNN). Viet and Zaki [39] developed an Artificial Neural Network (ANN) model to predict shell-based TPMS properties based on various geometric and material parameters, achieving high accuracy and efficiency. Furthermore, Ibrahimi et al. [40] reviewed several ML approaches for the design of sheet-based TPMS structures to optimize their design and successfully predict their mechanical performance.

In this work, a novel approach based on ANN is presented for the homogenization and prediction of elastic properties in TPMS-based structures. Specifically, this study focuses on shell-based (also known as sheet-based) structures due to significant advantages in terms of mechanical performance [12]. This framework then involves the generation of hybrid TPMS-based unit cells by combining the defining functions of four fundamental TPMS topologies, namely Primitive, Gyroid, Diamond, I-WP. While prior ANN-based studies typically focus on isolated or fixed TPMS topologies, this framework takes a significant step further by blending four fundamental TPMS into custom hybrid geometries. In doing so, it harnesses a larger design space to accurately capture anisotropic effects that inevitably arise when multiple parental geometries are merged.

The design space is represented as a tetrahedron whose vertices are represented by the four fundamental TPMS structures. A Design of Experiment (DOE) approach is used to generate the training dataset through a homogeneous mapping of this design space. FEA is used to calculate the stiffness matrix of the DOE points. ANN techniques are then applied to predict mechanical properties.

This combination of customized geometry generation, homogenization automation, and ANN modeling allows for extremely high regression accuracy, representing a substantial advancement in the design and application of TPMS-based structures. The proposed approach significantly broadens the scope of TPMS design and establishes a robust strategy for tailoring structural performance. As a result, it holds strong potential for lightweight engineering applications where multi-physics optimization, anisotropy control, and innovative geometry creation are crucial.

2 Methods

Figure 1 summarizes the workflow used in this study.

The methods used for each step of this workflow are detailed in the following subsections.

2.1 Hybrid cell design

In the present work, the design of TPMS in carried out with an implicit representation, leveraging the tools provided by the *nTop*© v5.10 software.

As discussed by Feng et al. [41], the exact definition of Triply Periodic Minimal Surfaces is derived from the Enneper-Weierstrass parametric representation and can be approximated using Fourier series expansions. The general implicit representation of a TPMS surface is provided in Eq. 2.1:

$$f(\boldsymbol{r}) = \sum_{k=1}^{K} A_k \cos\left(\frac{2\pi(\boldsymbol{h_k}\cdot\boldsymbol{r})}{\lambda_k} + P_k\right) = 0 \tag{2.1}$$

where A_k denotes the amplitude, λ_k denotes the period factor, $\boldsymbol{h_k}$ denotes the reciprocal space lattice vector and P_k denotes the phase of each goniometric term.

Whenever the coordinate system coincides with the Cartesian coordinate system, the statement $\boldsymbol{r} = (x, y, z)$ will be valid. Such a coordinate system will therefore be employed from this point forward.

By definition, a TPMS represents a three-dimensional surface without thickness. To obtain a solid structure, two level sets are introduced to define isosurfaces enclosing the solid region. The relation between the solid structure and the fundamental surface is described in detail by Fisher et al. [9]. In the implicit representation, the solid region comprised within the two level sets can be expressed by two inequalities, as shown by Eq. 2.2. Dealing with shell-based structures, the solid region comprised within the two level sets can thus be implicitly represented as shown by Eq. 2.2.

$$|f(x, y, z)| \leq \frac{t}{2} \tag{2.2}$$

where $f(x, y, z)$ is the function that approximates the implicit surface and t is a geometrical parameter describing the thickness of the TPMS.

The present work investigates the generation of novel hybrid TPMS structures by blending four fundamental geometries using a weighted combination, as shown in Eq. 2.3. The subscripts P, GY, D, and W are used throughout this work to refer respectively to the Schwarz Primitive, Schoen Gyroid, Schwarz Diamond, and Schoen I-Wrapped Package TPMS geometries.

$$\begin{aligned} f(x, y, z) = {} & c_P f_P(x, y, z) + c_{GY} f_{GY}(x, y, z) \\ & + c_D f_D(x, y, z) + c_W f_W(x, y, z) \end{aligned} \tag{2.3}$$

where f_P,f_{GY},f_D,f_W coincide with the fundamental surface definitions, detailed in Table 1 with the notations expressed in Eq. 2.4.

$$S_{ni} = \sin\left(\frac{2\pi n}{d_i} i\right) \qquad C_{ni} = \cos\left(\frac{2\pi n}{d_i} i\right) \tag{2.4}$$

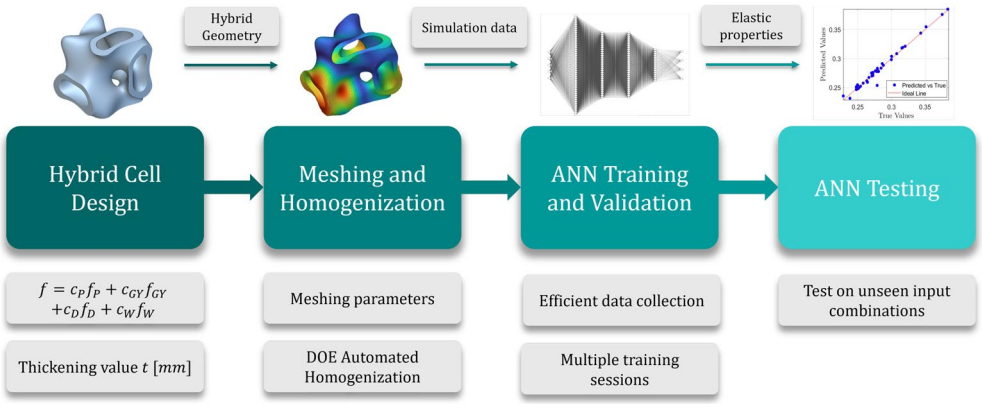

Fig. 1 Schematic diagram of the proposed workflow

Table 1 Implicit formulations of the four fundamental surfaces employed in this work

Fundamental TPMS	Implicit formulation
Primitive (P)	$f_P = C_x + C_y + C_z$
Gyroid (GY)	$f_{GY} = C_xS_y + C_yS_z + C_zS_x$
Diamond (D)	$f_D = S_xS_yS_z + S_xC_yC_z + C_xS_yC_z + C_xC_yS_z$
I-WP (W)	$f_W = 2(C_xC_y + C_yC_z + C_zC_x) - (C_{2x} + C_{2y} + C_{2z})$

In equation 2.4, i represents the general Cartesian coordinate (namely x, y, or z), d_i is the size of a unit cell along the i-direction and n is the number of periods of the goniometric function across the distance d_i.

The weighting coefficients c_P, c_{GY}, c_D and c_W in Eq. 2.3 are subject to the constraints in Eq. 2.5.

$$\begin{cases} c_P + c_{GY} + c_D + c_W = 1 \\ c_P, c_{GY}, c_D, c_W \geq 0 \end{cases} \tag{2.5}$$

In Eq. 2.3 each coefficient acts as a mixing weight on the signed-distance field of the corresponding parental TPMS. Because the four coefficients sum to unity (Eq. 2.5), the operation is equivalent to forming a convex combination of surfaces: when $c_{GY} = 1$ the implicit description collapses to a pure Gyroid, when $c_{GY} = 0.75$, $c_D = 0.25$ the resulting zero-level set has 75% of the geometric features of the Gyroid and 25% of the Diamond, and so on. A continuous morphing between the canonical TPMS is therefore provided in Fig. 2, which shows five unit cells along the straight line connecting the Gyroid ($c_{GY} = 1$) to the Diamond vertex ($c_D = 1$) of the design tetrahedron while keeping $c_P = c_W = 0$. Other families of cells (e.g. Primitive-I-WP blends) can be generated by traversing different edges or interior lines of the tetrahedron in exactly the same fashion.

The design space obtained by varying these four coefficients can be represented by a tetrahedron, as depicted in Fig. 3. Each vertex of the tetrahedron corresponds to a fundamental TPMS geometry, while any point within the tetrahedron uniquely corresponds to a hybrid combination of the four fundamental TPMS.

The tetrahedral representation shown in Fig. 3, suggests that the design space has 3 Degrees of Freedom (DoF). Specifically, each combination of the coefficients c_P, c_{GY}, c_D and c_W can be identified using three barycentric coordinates x^*, y^* and z^*. The relation between weighting

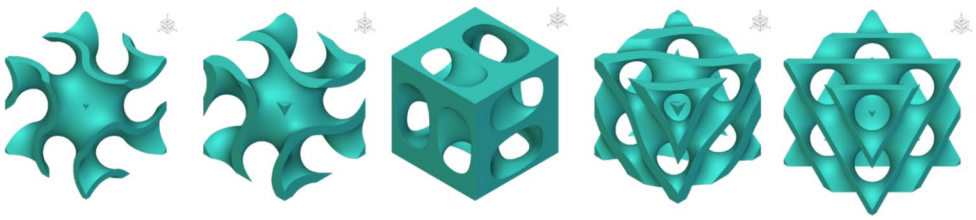

Fig. 2 Progressive blending from pure Gyroid ($c_{GY} = 1$) to pure Diamond ($c_D = 1$), obtained by linearly varying the two weights in steps of 0.25, i.e. $[c_P, c_{GY}, c_D, c_W] = [0, 1, 0, 0], [0, 0.75, 0.25, 0], [0, 0.5, 0.5, 0], [0, 0.25, 0.75, 0]$, and $[0, 0, 1, 0]$; the iso-parameter is fixed at $t = 0.7$

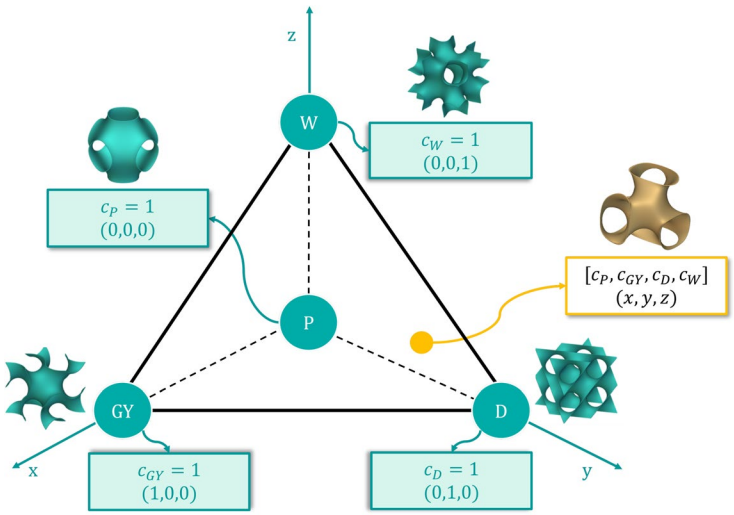

Fig. 3 Tetrahedral element representing the design space utilized for hybridization. Each corner corresponds to a distinct pureTPMS topology, while any point within the element is uniquely defined by its coordinates (x, y, z) and consequently by a set of four correlated merging coefficients: $[c_P, c_{GY}, c_D, c_W]$

coefficients and barycentric coordinates is made explicit in Eq. 2.6:

$$\begin{cases} c_{GY} = x^* \\ c_D = y^* \\ c_W = z^* \\ c_P = 1 - x^* - y^* - z^* \end{cases} \tag{2.6}$$

As a result, each solid hybrid configuration is distinctly represented by an array of four scalar values, i.e. $[x^*, y^*, z^*, t]$.

2.2 Homogenization

The linear elastic properties of each cell are retrieved through FEA using the Representative Volume Element (RVE) homogenization method. This approach consists of testing an elementary cell under different deformation conditions to extract the equivalent stiffness matrix of a fictitious material, which can then be used to simulate complex structures [33].

In this study, the AlSi10Mg aluminum alloy has been selected as the bulk material due to its prevalence in AM applications and its relevance in the literature regarding TPMS-based structures, as demonstrated by AlQayidi et al. [19]. An isotropic model of the material with a Young modulus of $E = 70,000$ MPa and Poisson ratio of $\nu = 0.33$ is used, based on values provided in the nTop library. It should be noted that TPMS-based cells are intended for AM production; thus, a certain degree of anisotropy may be introduced depending on the manufacturing process and inherent characteristics. As far as Laser Powder Bed Fusion (L-PBF) is concerned, unlike the resistance properties such as yield stress and ultimate strength, the elastic modulus remains relatively constant despite changes in layer thickness, hatch spacing, and scan strategy [42]. Specifically, the initial (elastic) stiffness of the material seems to be governed more by the native properties of the alloy rather than the processing-induced microstructural variations. Therefore, the hypothesis of isotropic material is assumed to be acceptable for determining the properties of a linear elastic RVE. It should be noted that an accurate characterization of the bulk material is not within the scope of this paper. The focus of this study is the definition of a method to predict the geometry-based variations of mechanical properties in hybrid TPMS. The methodology outlined herein can be readily adapted for application to any material of interest.

An initial triangular surface mesh of each TPMS unit cell was generated so that every node lays within 0.10 mm of the analytical surface. The *sharpening* routine in nTop was subsequently invoked to reconstruct sharp geometric features, followed by the *remesh* function, which removed minor defects and consolidated elements. The refined surface was then converted into a tetrahedral volume mesh with maximum edge length h and a growth rate of 1.1.

Figure 4adocuments the influence of h on the homogenized axial modulus C_{11}. For all four parent topologies the response plateaus: decreasing h from 0.12 mm to 0.07 mm alters C_{11} by less than 1 %. Accordingly, $h = 0.10$ mm was selected for every DOE homogenization run, and the surface-mesh tolerance was fixed to the same value in order to preserve geometric fidelity without unnecessary over-refinement. Comparable convergence behavior was obtained for the remaining stiffness coefficients. A representative volume mesh of a hybrid cell is illustrated in Fig. 4b

To account for the influence of adjacent units on the elastic behavior, Periodic Boundary Conditions (PBC) were applied to the cell for FEA. These conditions aim to replicate the case of an infinite pattern of elementary units.

PBC formulation is based on the decomposition of the RVE boundary and a kinematic constraint. The

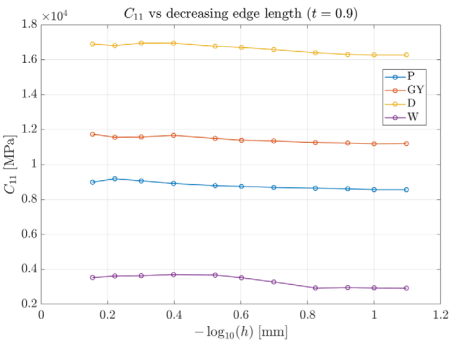

(a) Mesh-convergence curve for the axial modulus C_{11} ($t = 0.9$).

(b) Representative hybrid-cell mesh generated with the parameter set $[c_P, c_{GY}, c_D, c_W, t] = [0.3, 0.3, 0.3, 0.1, 0.5]$.

Fig. 4 **a** Convergence of the homogenized axial modulus C_{11} with decreasing tetrahedral edge length h; **b** final hybrid-cell mesh adopted for the homogenization study

displacement field at any point of the boundary can be decomposed into a macro-displacement $\hat{\boldsymbol{u}}$ and a micro-displacement $\tilde{\boldsymbol{u}}$, as described by Eq. 2.7.

$$\boldsymbol{u}(\boldsymbol{x}) = \hat{\boldsymbol{u}}(\boldsymbol{x}) + \tilde{\boldsymbol{u}}(\boldsymbol{x}) = \boldsymbol{u}_0 + \boldsymbol{H} \cdot \boldsymbol{x} + \tilde{\boldsymbol{u}}(\boldsymbol{x}) \tag{2.7}$$

where $\boldsymbol{H}$ is the macroscopic displacement gradient and coincides with the macroscopic strain ϵ. This is enforced by kinematically constraining the difference in the displacements of paired nodes, as expressed by Eq. 2.8.

$$\tilde{\boldsymbol{u}}(\boldsymbol{x} + a\lambda_i \boldsymbol{e}_i) = \tilde{\boldsymbol{u}}(\boldsymbol{x}) \quad \Rightarrow \quad \boldsymbol{u}(\boldsymbol{x}^+) - \boldsymbol{u}(\boldsymbol{x}^-) = a\boldsymbol{H} \cdot \boldsymbol{n} \tag{2.8}$$

where:

- $\boldsymbol{x}^+$ and $\boldsymbol{x}^-$ are two points on opposite boundaries of the RVE [30], which are uniquely connected due to periodicity and are characterized by a normal vector $\boldsymbol{n}^+ = -\boldsymbol{n}^- = \boldsymbol{n}$,
- a is the size of the cubic unit cell (which coincides with the RVE),
- λ_i is any integer number,
- $\boldsymbol{e}_i$ is a principal direction of the material.

For example, PBC can be explicitly stated for a simple scenario such as the uniaxial deformation along the z-axis. Assuming the imposed strain being ϵ_{zz} and the center of the coordinate system being the center of the cell, constraints of PBC are as in Eq. 2.9.

$$\begin{array}{lll} u_x|_{x=-\frac{a}{2}} - u_x|_{x=\frac{a}{2}} = 0 & u_x|_{y=-\frac{a}{2}} - u_x|_{y=\frac{a}{2}} = 0 & u_x|_{z=-\frac{a}{2}} - u_x|_{z=\frac{a}{2}} = 0 \\ u_y|_{x=-\frac{a}{2}} - u_y|_{x=\frac{a}{2}} = 0 & u_y|_{y=-\frac{a}{2}} - u_y|_{y=\frac{a}{2}} = 0 & u_y|_{z=-\frac{a}{2}} - u_y|_{z=\frac{a}{2}} = 0 \\ u_z|_{x=-\frac{a}{2}} - u_z|_{x=\frac{a}{2}} = 0 & u_z|_{y=-\frac{a}{2}} - u_z|_{y=\frac{a}{2}} = 0 & u_z|_{z=-\frac{a}{2}} - u_z|_{z=\frac{a}{2}} = \epsilon_{zz} \cdot a \end{array} \tag{2.9}$$

where u_x, u_y, u_z are the displacement components along the x, y, z axes, respectively.

It is important to note that the periodicity condition is representative of cell behavior under the hypothesis of a sufficiently large number of neighboring units [43]. When employing cells for a real component, the effects on the boundaries must be taken into account. This point must also be considered in the experimental validation of homogenization [44]. This issue is not covered in this study and is left as a future extension.

The force reactions on the constrained boundary nodes allow for retrieving the stress in different directions which, assuming a unitary strain, correspond to the terms of the stiffness matrix.

While certain TPMS geometries-such as the Gyroid, Diamond, and Fischer-Koch S-possess an inherent threefold rotational symmetry at the unit-cell scale, Lu et al. [45] demonstrated through numerical homogenization that their corresponding scaffold structures manifest mechanical behaviors consistent with cubic symmetry. In other words, despite the geometrical complexity and lower-order symmetry (threefold rotational symmetry) inherent in individual unit cells, when subjected to periodic boundary conditions representative of an infinite structure, the macroscopic elastic response simplifies significantly, reducing to cubic mechanical symmetry. This distinction ensures the feasibility of neglecting additional anisotropic terms in the stiffness matrix when modeling TPMS-based scaffolds. Although a single Gyroid unit cell alone does not geometrically satisfy cubic symmetry, its repeated and periodic arrangement leads to a macroscopic mechanical response that indeed satisfies cubic symmetry conditions. According to this hypothesis, the stiffness matrix would have three independent elastic constants due to the symmetry in the material properties, specifically C_{11}, C_{12}, C_{44}. This implies that the material behaves identically when deformed along any of the three principal axes (x, y, z). As suggested by Chen et al. [46], TPMS-based structures predominantly exhibit orthotropic behavior, meaning that the stiffness matrix requires the calculation of all the elements highlighted in blue in Fig. 5.

Nevertheless, previous research such as Chen et al. [25] demonstrated that, for hybrid cells, some of the stiffness constants that should be negligible under the cubic symmetry hypothesis, namely those indicated as *anisotropic terms* in Fig. 5, actually exceed 1% of the maximum element in the matrix. This result is confirmed in this study. Therefore, an anisotropic material model here is used for RVE.

Under the general assumption of fully anisotropic behavior of the hybrid cell, 6 elementary simulations (3 normal and 3 shear strains) are needed to retrieve the 21 independent coefficients of the stiffness matrix.

To quantify the degree of anisotropy for each cell, the Zener ratio (A_Z), originally introduced by Zener [47], is calculated as given in Eq. 2.10.

$$A_Z = \frac{2C_{44}}{C_{11} - C_{12}} \tag{2.10}$$

For a perfectly isotropic material $A_Z = 1$; the higher the value of A_Z, the more the elastic response of the cell is anisotropic.

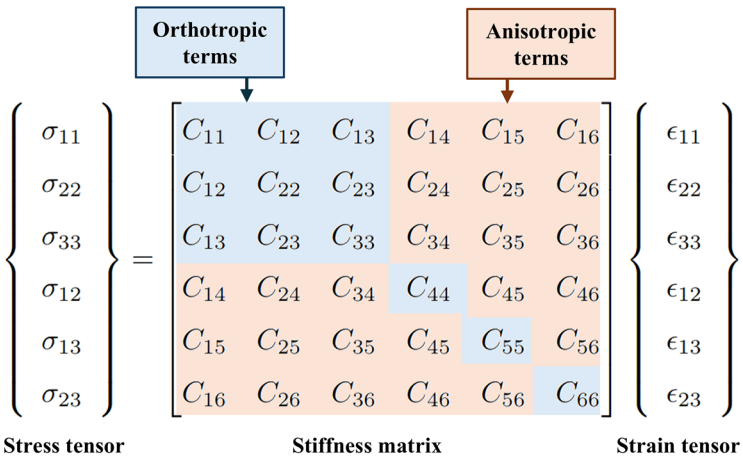

Fig. 5 Highlighting of orthotropic and anisotropic terms of the stiffness matrix

2.3 Design of the experiment

A DOE approach is used to build the database for training the ML model to predict the elastic properties of hybrid structures. In particular, a Full Factorial (FF) DOE is used varying the four independent geometrical parameters of the cell (x^*,y^*,z^* and t) are varied in a FF. Barycentric coordinates have been varied in the range [0, 1] with a step of 0.125, namely with $L = 9$ levels. The isoparameter value t is varied in the interval [0.5, 1.2] with a step 0.1, namely with $L_t = 8$ levels. This interval is chosen based on preliminary observations to obtain realistic cell geometries. The total number of experiments N_x, calculated as in Eq. 2.11, is equal to 1320:

$$N_x = L_t\left(\frac{L!}{3!(L-3)!}\right) \tag{2.11}$$

A FF-based grid provides orthogonality but inherently leads to significant voids within the tetrahedral domain due to its rigid, crystalline structure. These regular patterns may inadvertently introduce artificial symmetries, potentially misleading non-parametric learning algorithms. To mitigate this issue, the structured grid has been augmented by adding 300 additional sampling points, drawn randomly from a continuous distribution over the same barycentric space. This hybrid sampling strategy, as depicted in Fig. 6, thus merges the statistical advantages of structured experimental designs with the variance-reducing characteristics of space-filling random approaches. Similar hybrid approaches have been employed successfully in the literature to enrich the dataset and enhance machine learning model performance [26].

The simulations were programmatically run via Python script by using the nTop Application programming interface (API). The extracted output parameters are the 21 independent coefficients of the stiffness matrix, the A_Z value, and the volume fraction Volume Fraction (VF) of each cell.

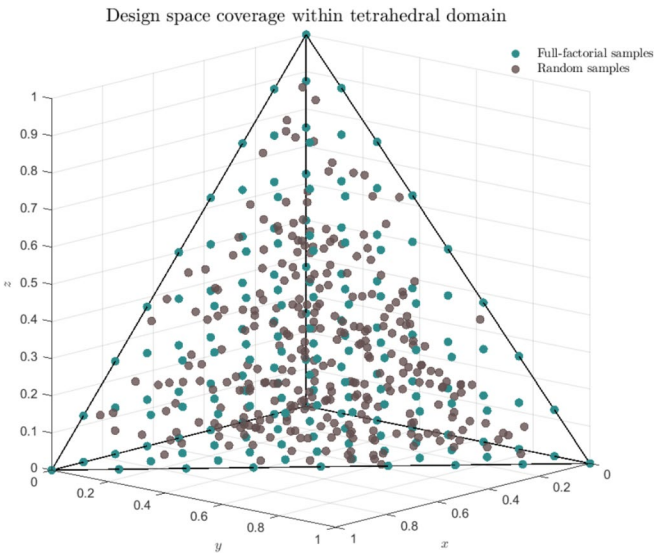

Fig. 6 Design space coverage within the tetrahedral domain. Full-factorial samples form a structured grid and are evaluated at discrete values of $t \in [0.5, 1.2]$. Random samples are drawn uniformly from the domain and assigned random t values within the same range

All homogenization jobs were run on a consumer laptop with Windows 11 Home (build 26100), an Intel Core i7-1165G7 CPU (4 cores/8 threads, 2.8 GHz) and 16 GB RAM. A single configuration-including geometry generation, three-stage meshing and six finite-element load cases-required on average 11 minutes of wall time, of which roughly 200 s were devoted to the meshing stage.

2.4 ANN training process

The inputs of the network are the geometrical parameters of the cell, namely $[t, c_P, c_{GY}, c_D, c_W]$. One separate ANN is built to predict each of the 23 output parameters, i.e. $C_{11}, C_{12}, C_{13}, C_{14}, C_{15}, C_{16}, C_{22}, C_{23}, C_{24}, C_{25}, C_{26}, C_{33}, C_{34}, C_{35}, C_{36}, C_{44}, C_{45}, C_{46}, C_{55}, C_{56}, C_{66}, VF, A_Z$. This strategy results more efficiently in the prediction than a single network with multiple outputs, as demonstrated by several studies such as Wang et al. [27].

Ahead of ML elaboration, all the data are normalized in the range [0, 1].

Linear ANN networks were implemented using the MLPRegressor function from the Python Scikit-Learn library. These models consist of an input layer of 5 neurons, four hidden layers with 256, 128, 128, and 32 neurons, an output layer with a single neuron, as schematically illustrated in Fig. 7. Rectified Linear Unit (ReLU) activation was used in the hidden layers. This architecture was chosen for being the most promising after preliminary tests.

75% of the homogenization data was used to train the ANN, while the remaining 25% was used for validation. The model was subsequently tested on 80 randomly extracted samples, which were explicitly excluded from the training dataset.

Adaptive Moment Estimation (AdaM) optimizer has been used for back propagation. The training configuration includes an initial learning rate of 0.001 and incorporates L2 regularization (weight decay) to mitigate overfitting. Finally, early stopping is implemented to halt training if the validation error fails to improve, with training capped at a maximum of 1000 iterations. These measures collectively enhance the robustness and generalization capability of the model [48].

To further substantiate that overfitting has been effectively mitigated, the learning curve for the primary stiffness term C_{11} has been examined, as shown in Fig. 8. The training loss decreases steadily over the epochs, while the validation coefficient of determination R^2 correspondingly rises and then plateaus, without any subsequent divergence or decline. The close alignment of training and validation metrics-evidenced by the absence of a widening gap between the two curves-confirms that the model converges without overfitting, thereby validating the efficacy of the adopted L2 regularization and early?stopping strategy. Similar trends were observed across all other output parameters.

Performance in the test data has been evaluated using common correlation metrics such as the normalized Root Mean Square Error (*RMSE*) and the coefficient of determination (R^2). In addition to the standard training and prediction procedures, a control for outlier detection has been integrated into the model to identify and analyze predictions that exhibit significant deviations from the actual values. This check operates by calculating the relative error for

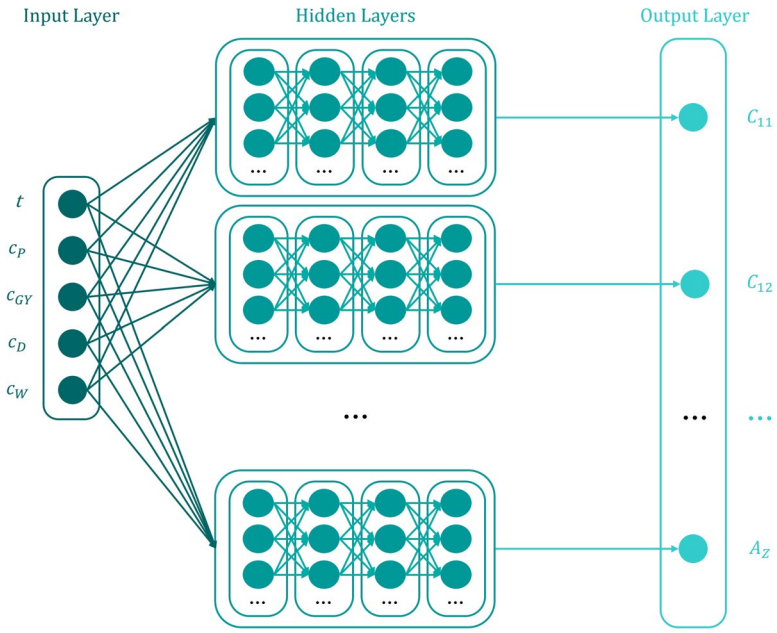

Fig. 7 Schematic diagram of the chosen ANN architecture. As visible, all output parameters are calculated in separate identical networks

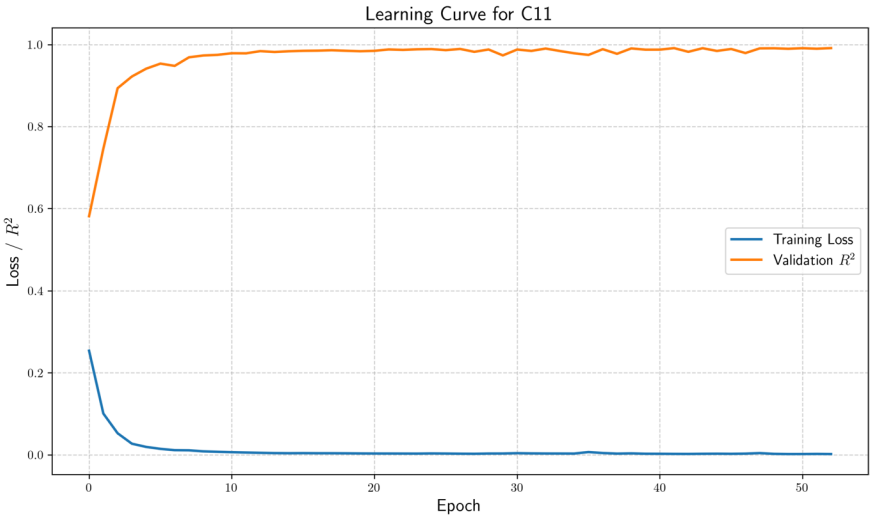

Fig. 8 Learning curve for C_{11}: training loss versus validation R^2 over epochs

each prediction and signaling if this value exceeds a defined threshold of 10%.

To further validate the robustness and generalization capability of the implemented neural network, a k-fold cross-validation approach was introduced, with $k = 5$. This methodology partitions the dataset into five subsets of equal size, sequentially using each subset as a validation set while training the model on the remaining data. The obtained R^2 scores across folds for representative mechanical properties such as C_{11} demonstrated consistently high accuracy (e.g., $\bar{R}^2 = 0.9815 \pm 0.0077$), confirming the stability and reliability of the ANN in predicting elastic coefficients across different regions of the design space. This additional evaluation metric complements the original train/validation/test split and provides a statistically grounded estimate of model performance, thereby enhancing the methodological soundness of the proposed predictive framework.

3 Results and discussion

3.1 Homogenization Results

In Fig. 9, the first element of the stiffness matrix (C_{11}) is plotted against the Volume Fraction (VF) of the cell.

In Fig. 9, it can be seen that a generally exponential change in C_{11} can be observed while increasing VF. This is an expected result in light of the existing literature. For instance, researchers such as Patel et al. demonstrated how the Gibson- Ashby Model (GAM) can be utilized to validate the mechanical performance of TPMS structures by benchmarking experimental results against theoretical predictions [26].

The GAM provides a fundamental theoretical framework for understanding the mechanical properties of cellular solids and has been extensively applied to TPMS-based

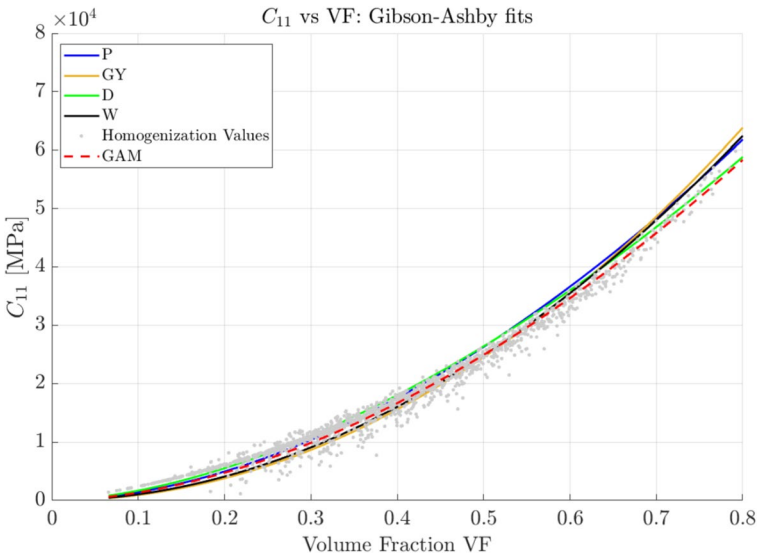

Fig. 9 Variation of C_{11} stiffness with volume fraction VF

structures [49]. The model correlates the mechanical properties of cellular materials with their relative density, as evidenced by Eq. 3.1.

$$P = C\left(\frac{\rho_{cell}}{\rho_{bulk}}\right)^{n} \tag{3.1}$$

where:

- P is a material property,
- $\frac{\rho_{cell}}{\rho_{bulk}}$ is the relative density, which mathematically coincides with the volume fraction under the assumption of perfect or ideal structures (i.e., defects and micro-porosities are disregarded),
- C and n are material constants which are interpolated from the experimental data.

The extracted GAM, which has been calculated using a MATLAB script, is in turn plotted in Fig. 9. The four GAM curves for the fundamental TPMS structures are also shown to visualize their relation with mixed cells. Consistently with classical cellular-solid theory, the power-law fit explains most of the variance of the axial modulus ($R^2 = 0.9833$). This result confirms that the global stiffness is governed mainly by relative density, while the detailed topology plays a secondary role. Recent experimental studies corroborate that sheet-based TPMS structures such as Gyroid or Diamond exhibit near-stretch-dominated behavior with $n \approx 1$, whereas strut-based Kelvin or skeletal-based TPMS structures show exponents between 1.5 and 2, signaling mixed or bending-dominated modes. For the present hybrid dataset the Gibson-Ashby fit of C_{11} yields an exponent $n = 1.811$, which sits closer to the bending-dominated limit and highlights the strong influence of Primitive-rich regions in the design space. Since hybrid cells therefore blend these different modes, the GAM should be regarded as a first-order, mass-based estimate rather than a universal predictor, in line with the warning already expressed by Guo et al. [50].

The limitation becomes obvious when one turns to anisotropic coupling terms. Figure 10 shows that the same GAM fit totally fails to capture the evolution of C_{14}. Off-diagonal constants are extremely sensitive to the presence of local bending in Primitives and to the loss of three-fold symmetry that occurs when parental cells are combined, issues that are outside the scope of the one-parameter GAM formulation. Similar discrepancies between GAM predictions and measured shear/anisotropic properties have been observed for both metal TPMS structures produced by L-PBF [51] and

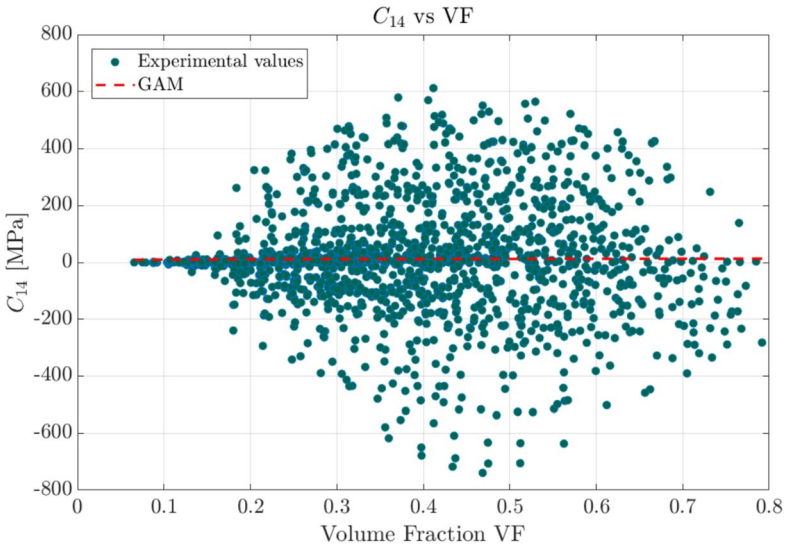

Fig. 10 Variation of C_{14} stiffness with volume fraction VF

Table 2 R^2 scores for the GAM; entry in row i, column j is $R^2(C_{ij})$. Displayed is only the upper triangle, since the regression matrix is symmetric, i.e. $R^2(C_{ij}) = R^2(C_{ji})$

$i \backslash j$	1	2	3	4	5	6
1	0.9833	0.9525	0.9526	$< 10^{-4}$	0.0671	0.0070
2		0.9833	0.9526	0.0070	$< 10^{-4}$	0.0673
3			0.9833	0.0674	0.0070	$< 10^{-4}$
4				0.9833	0.0519	0.0525
5					0.9833	0.0522
6						0.9833

polymer Gyroids fabricated by Fused Deposition Modeling (FDM) [52].

In short, the GAM curve in Fig. 9 can be retained as a convenient preliminary yardstick: it provides a fast density-modulus estimate and it helps to identify which stiffness components are primarily density-controlled (e.g. C_{11}) and which ones are geometry-controlled (e.g. C_{14}). This can be further validated by Table 2, which summarizes the R^2 of the GAM when applied to the different elements of the stiffness matrix.

While the axial modulus therefore scales smoothly with VF, the degree of elastic anisotropy changes much more abruptly across the design space. This can be shown considering the Zener index A_Z, which is plotted against the VF in Fig. 11.

As illustrated in Fig. 11, the results reveal a broad range of Zener index values at lower densities (approximately below 30%), spanning from nearly isotropic ($A_Z \approx 1$) to highly anisotropic ($A_Z > 3$). This variability suggests that the structural response is significantly influenced by directional properties at lower densities, which are further affected by the specific geometric configurations. Certain configurations demonstrate a greater isotropic behavior compared to others.

Moreover, as the volume fraction increases, the anisotropy index exhibits a gradual stabilization towards approximately $A_Z = 1$. This indicates that as the quantity of the utilized material increases, the structures become more isotropic in their mechanical response, approaching the behavior of bulk material, which has been previously assumed to be perfectly isotropic. This phenomenon can be attributed to a more homogeneous distribution of stresses that occurs with an increase in material utilization. Furthermore, as evidenced by the polynomial interpolations of the parental cells, Primitive structures typically exhibit greater anisotropy, particularly at lower densities. This behavior is attributed to a bending-dominated deformation mechanism, which becomes prominent as the structure becomes thinner and is accompanied by significant lateral deformations under axial loading [13]. In contrast, Gyroid and Diamond structures are primarily stretching-dominated and likely exhibit lower anisotropy even at lower values of the volume fraction. Notably, recent findings by Chen et al. [53] on hybrid TPMS sheet-based designs further confirm that combining bending-dominated architectures can enhance crashworthiness and energy absorption capabilities, illustrating how mixing topologies can exploit their complementary strengths.

Finally, an additional analysis of the orthotropic behavior of these structures has been conducted. As suggested by Chen et al. [46], TPMS-based structures predominantly exhibit orthotropic behavior; however, some of the stiffness constants appear to be non-negligible. The threshold to determine non-negligibility was set when anisotropic terms in Fig. 5 exceed 1% of the maximum stiffness component in the matrix. As highlighted in Fig. 12, the results of this study corroborate the observations by [46], as the number of instances in which this occurred exceeds the acceptable numerical uncertainty of the simulations. As indicated by previous studies, this phenomenon might be explained by the symmetry of the trigonometric functions, which may be lost in the weighted sum of parental functions.

To further illustrate the symmetry-breaking anisotropy introduced by hybrid blending, a full-surface map of the effective Young's modulus has been generated on a representative 62.5% Primitive - 37.5% Diamond cell (Fig. 13c).

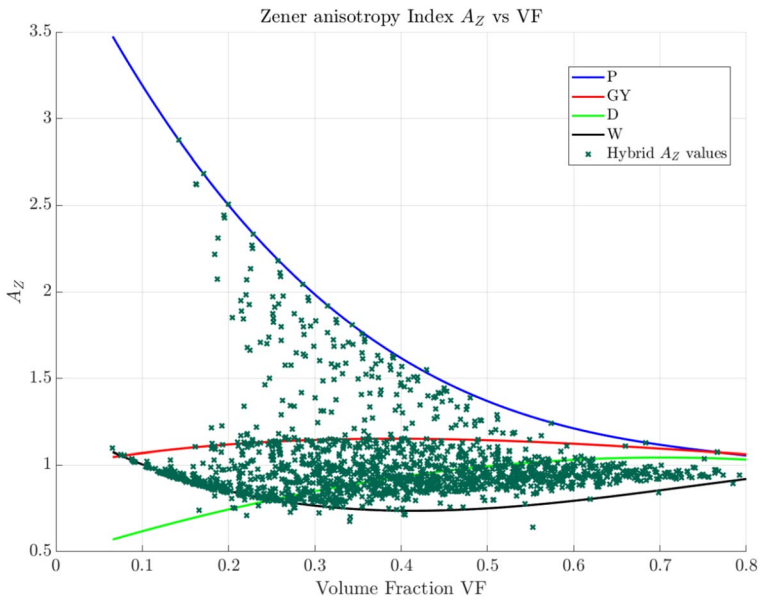

Fig. 11 Comparison of anisotropy Zener index A_Z of hybrid TPMS structures with parental TPMS trends

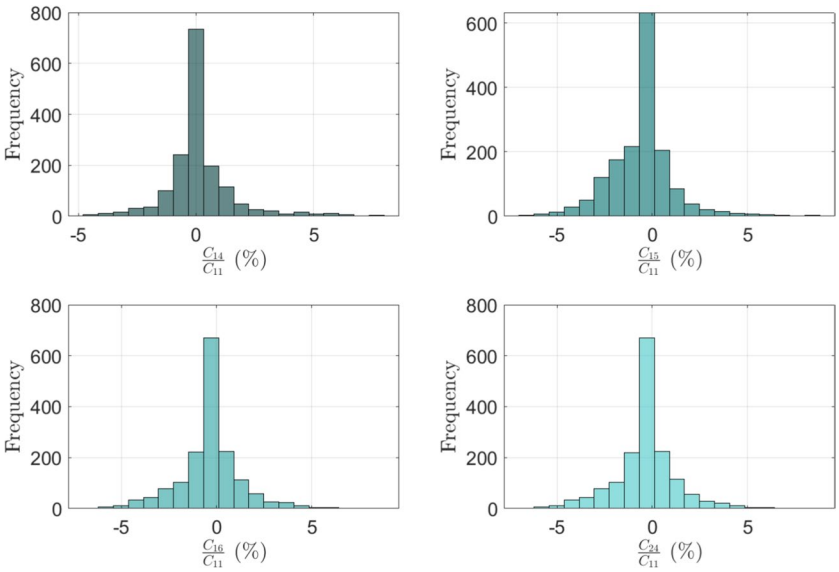

Fig. 12 Examples of off-diagonal terms deviating from the orthotropic assumption

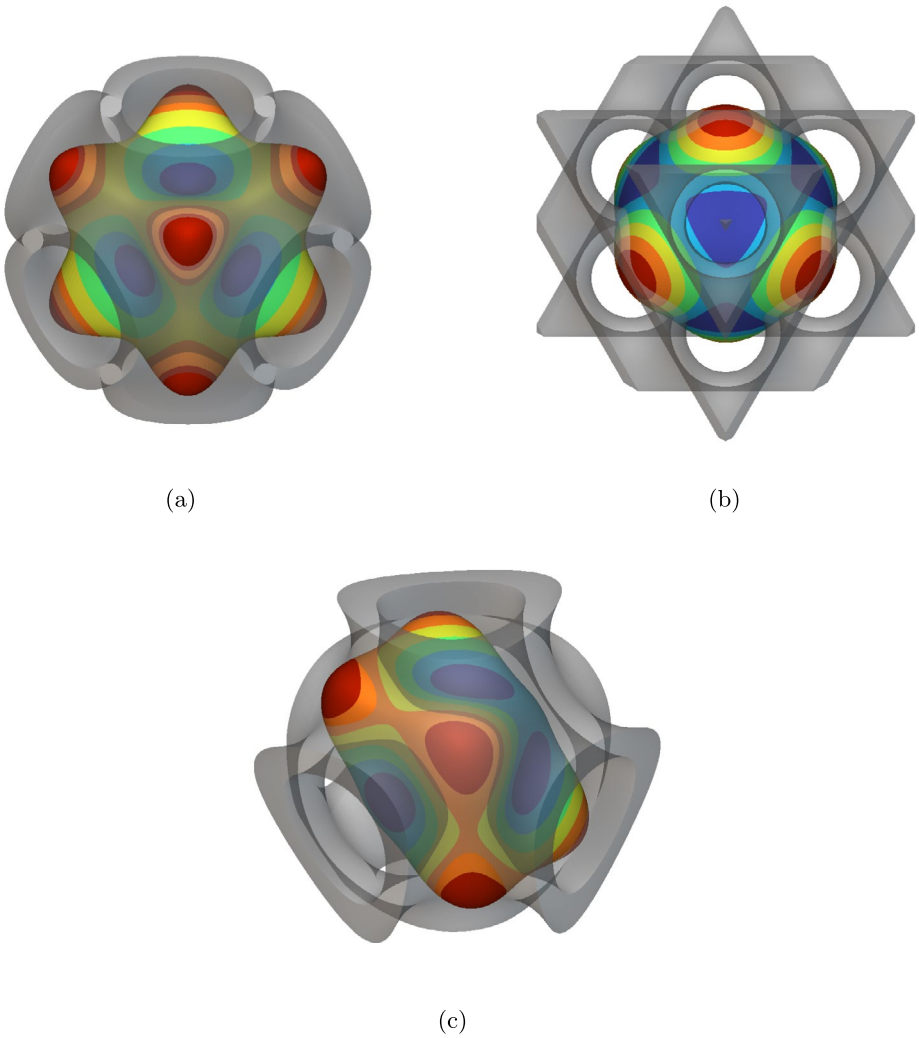

Fig. 13 Full surface maps of the effective Young's modulus for three different TPMS-based unit cells at $t = 0.5$. Figure 13ashows a Primitive cell ($[c_P, c_{GY}, c_D, c_W] = [1, 0, 0, 0]$), Fig. 13ba Diamond cell ([0, 0, 1, 0]), and Fig. 13ca hybrid Primitive-Diamond cell ([0.625, 0, 0.375, 0])

In this contour plot, the stiffness maxima appear as distinct lobes that do not repeat at the 90° or 120° intervals characteristic of cubic or three-fold rotational symmetry. As evidenced by Fisher et al. [9], the Diamond cell exhibits a nearly circular stiffness envelope with only modest six?lobed deviations (Fig. 13b), reflecting its residual cubic symmetry. In stark contrast, the Primitive cell shows a pronounced eight?pointed star pattern, with stiffness peaks along the cube diagonals, characteristic of its bending-dominated walls (Fig. 13a). By comparison, the representative hybrid combination shown in Fig. 13cdisplays irregular, non-repeating lobes that neither conform to the six-fold symmetry of the Diamond nor the six-fold symmetry of the Primitive. This irregular envelope provides direct visual proof that weighted blending of two symmetric parental TPMS topologies breaks down their original symmetry, yielding a truly anisotropic, symmetry-broken structure.

Overall, these results prove that, even if the GAM can effectively depict the trend of linear elastic properties, it does not allow for an accurate prediction of the punctual values. This is due to the effect of anisotropy introduced by different cell morphology. This confirms the need for more accurate regression models capable of effectively forecasting the stiffness matrix of a generic hybrid cell in the design space.

3.2 ANN prediction results

Table 3 summarizes the R^2 scores of the network model for all the terms of the stiffness matrix.

As can be observed, the model exhibits lower R^2 values for the anisotropic terms, namely those assumed to be equal to zero under the orthotropic hypothesis. This result can be explained if considering that the values of these terms are negligible in most of the cases, so the network has only few cases to learn from. On the other hand, it can be observed that the accuracy of the prediction on all the orthotropic terms is above 99.3%. This confirms the validity of the method to achieve an accurate estimation of the cell stiffness. By comparing Table 3 and Table 2, it can be observed

Table 3 R^2 scores for the ANN regression-coefficient matrix; entry in row i, column j is $R^2(C_{ij})$. Displayed is only the upper triangle, since the regression matrix is symmetric, i.e. $R^2(C_{ij}) = R^2(C_{ji})$

$i \backslash j$	1	2	3	4	5	6
1	0.9934	0.9919	0.9910	0.9725	0.9795	0.9717
2		0.9937	0.9919	0.9811	0.9766	0.9804
3			0.9935	0.9764	0.9746	0.9778
4				0.9940	0.9806	0.9759
5					0.9957	0.9738
6						0.9953

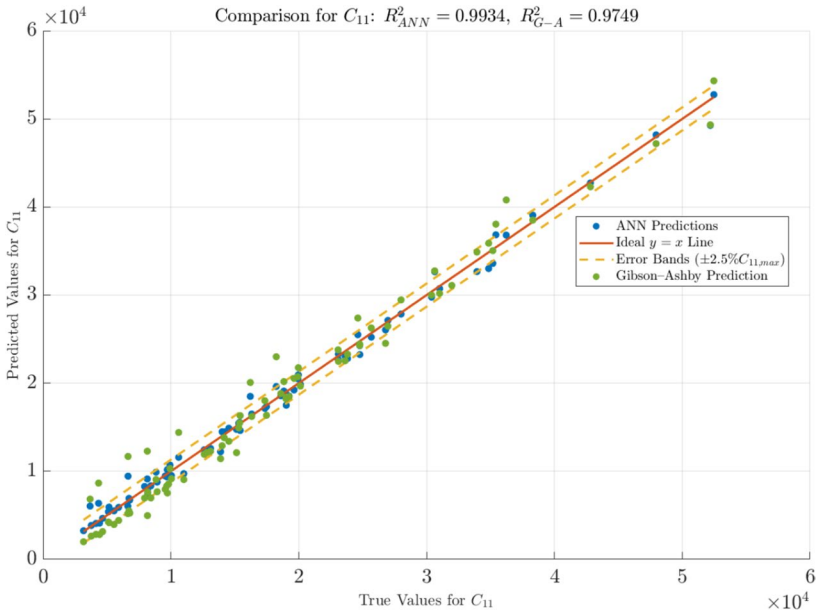

Fig. 14 Comparison of predicted and homogenized (true) C_{11} values, with error boundaries defined by $y = x \pm 2.5\%\ C_{11,max}$

that the ANN leads to a significant improvement in the accuracy of the regression on the orthotropic terms. However, the main advantages of the ANN can be appreciated on the anisotropic terms, where the accuracy of the GAM is practically null. This is a pivotal result, as it demonstrates that this method is able to predict the anisotropy introduced by mixing the fundamental cells.

The R^2 score obtained on VF is equal to 0.9978, highlighting a very high correlation. This can be explained by considering the quasi-linear correlation between VF and the iso-parameter t, as indicated by Fisher et al. [9]. As the volume fraction is the only parameter considered by the GAM, this accuracy confirms that the ANN can effectively describe the trend of that model. As far as A_Z is concerned, the calculated R^2 is equal to 0.9778. This confirms that, besides the effect of the cell density, the network allows for catching the geometry-induced anisotropy of the structure, thus leading to a major improvement in the prediction.

Evidently, it is crucial to note that the evaluation of these results has thus far been based on average performance metrics such as R^2 and $RMSE$. However, these metrics do not account for the variability in performance across individual combinations. To address this limitation, the model has been designed to effectively identify outliers, enabling a more comprehensive assessment of its robustness in handling anomalous cases. Outliers were defined as instances where the absolute deviation from the homogenization target value exceeded ±2.5% of the maximum target value. As an example, Fig. 14 compares the results of the predictions obtained through GAM and ANN in the C_{11} term of the stiffness matrix.

As can be observed, the use of ANN dramatically reduces the number of outliers (i.e. points outside the 2.5% error bands), thus showing an additional benefit beyond the increase in R^2. A similar trend is observed with the other terms of the matrix.

These outliers were analyzed in relation to their input coefficients to identify potential patterns. Multiple iterations of parallel training processes did not reveal any specific patterns among the identified outliers, which instead appeared to be related to the random selection of testing samples. The repeatability of the results over multiple replications of the training and validation process highlights the effectiveness and reliability of the DOE-based data sampling approach, which demonstrated resilience against systematic biases.

4 Conclusion

This work has proposed a novel framework for the generation, homogenization, and predictive modeling of Triply Periodic Minimal Surface-based structures, combining numerical simulations and Machine Learning techniques. It has successfully demonstrated the potential of Primitive, Gyroid, Diamond, and I-WP cells to optimize mechanical properties for various engineering applications. Hybridization therefore widens the design horizon far beyond the four canonical topologies, delivering a continuous spectrum of feasible geometries that can be matched to specific performance targets without bespoke optimization loops. The presented approach holds considerable promise across aerospace, automotive, biomedical, and energy-absorption fields due to its capability to customize and optimize lightweight structures.

The results demonstrated that the Artificial Neural Network allows for an effective prediction of all the terms of the stiffness matrix for a generic hybrid structure. This precise yet lightweight surrogate thus replaces time-consuming Finite Element-based homogenization in the iterative design cycle, enabling rapid screening or real-time optimization. Moreover, when compared to the Gibson-Ashby Model, the Artificial Neural Network significantly improves accuracy (in terms of R^2) for coefficients essential to establishing an orthotropic model of the cell. Another major finding is that the Artificial Neural Network, unlike the Gibson-Ashby Model, is able to capture the anisotropic behavior which originates from mixing fundamental Triply Periodic Minimal Surfaces. This can be seen in the regression of the Zener ratio, as well as in the prediction of the anisotropic elements of the stiffness matrix. Additionally, the Artificial Neural Network approach has been demonstrated to substantially reduce the number of outliers if compared to the Gibson-Ashby Model.

Overall, this research demonstrates that an Artificial Neural Network trained on a suitably designed set of equidistant points can robustly predict the linear elastic properties of complex cellular structures obtained by hybridization of fundamental Triply Periodic Minimal Surfaces. Future work includes validating the model experimentally and through large-scale finite-element simulations, capturing the effects of additive-manufacturing defects, material anisotropy, and non-linear behavior. In parallel, authors are extending the framework to functionally graded lattices in which topology and relative density vary smoothly across the part. Combining these graded-geometry studies with forthcoming test data will tighten the agreement between simulation and reality and further reinforce the proposed design pipeline.

Funding Open access funding provided by Alma Mater Studiorum - Università di Bologna within the CRUI-CARE Agreement.

Data availability The complete homogenization results dataset can be accessed at https://doi.org/10.17605/OSF.IO/C2HR4.

References

1. Huang WS, Ning HY, Li N, Tang GH, Ma Y, Li Z, Nan XY, Li XH (2024) Thermal-hydraulic performance of TPMS-based regenerators in combined cycle aero-engine. Appl Thermal Eng. https://doi.org/10.1016/j.applthermaleng.2024.123510
2. Zhang S, Da D, Wang Y (2022) TPMS-infill MMC-based topology optimization considering overlapped component property. Int J Mech Sci. https://doi.org/10.1016/j.ijmecsci.2022.107713
3. Liu W, Zhang Y, Lyu Y, Bosiakov S, Liu Y (2023) Inverse design of anisotropic bone scaffold based on machine learning and regenerative genetic algorithm. Front Bioeng Biotechnol. https://doi.org/10.3389/fbioe.2023.1241151
4. Yin H, Zhang W, Zhu L, Meng F, Liu J, Wen G (2023) Review on lattice structures for energy absorption properties. Composite Struct. 304:116397. https://doi.org/10.1016/j.compstruct.2022.116397
5. Gado MG, Al-Ketan O, Aziz M, Al-Rub RA, Ookawara S (2024) Triply periodic minimal surface structures: design, fabrication, 3D printing techniques, state-of-the-art studies, and prospective thermal applications for efficient energy utilization. Energy Technol. https://doi.org/10.1002/ente.202301287
6. Kladovasilakis N, Tsongas K, Tzetzis D (2021) Mechanical and fea-assisted characterization of fused filament fabricated triply periodic minimal surface structures. J Composites Sci. https://doi.org/10.3390/jcs5020058
7. Shi X, Liao W, Li P, Zhang C, Liu T, Wang C, Wu J (2020) Comparison of compression performance and energy absorption of lattice structures fabricated by selective laser melting. Adv Eng Mater. https://doi.org/10.1002/adem.202000453
8. Xin J, Wu W, Cao K, Li C, Peng Y, Du C, Shan B (2024) Enhanced molding and mechanical properties of SiC-based ceramic lattice structures via digital light processing. Ceramics Int. 50(21, Part B):42352–42362. https://doi.org/10.1016/j.ceramint.2024.08.081
9. Fisher JW, Miller SW, Bartolai J, Simpson TW, Yukish MA (2023) Catalog of triply periodic minimal surfaces, equation-based lattice structures, and their homogenized property data. Data Brief. https://doi.org/10.1016/j.dib.2023.109311
10. Teng F, Sun Y, Guo S, Gao B, Yu G (2022) Topological and mechanical properties of different lattice structures based on additive manufacturing. Micromachines. https://doi.org/10.3390/mi13071017
11. Zhang L, Feih S, Daynes S, Shuai C, Wang M, Wei J, Lu W-F (2018) Energy absorption characteristics of metallic triply periodic minimal surface sheet structures under compressive loading. Addit Manuf. https://doi.org/10.1016/j.addma.2018.08.007
12. Al-Ketan O, Rowshan R, Abu Al-Rub RK (2018) Topology-mechanical property relationship of 3D printed strut, skeletal, and sheet based periodic metallic cellular materials. Addit. Manuf. 19:167–183. https://doi.org/10.1016/j.addma.2017.12.006
13. Abueidda D, Elhebeary M, Shiang A, Pang S, Abu Al-Rub R, Jasiuk I (2019) Mechanical properties of 3D printed polymeric Gyroid cellular structures: experimental and finite element study. Mater Design 165:107597. https://doi.org/10.1016/j.matdes.2019.107597
14. Feng J, Liu B, Lin Z, Fu J (2021) Isotropic porous structure design methods based on triply periodic minimal surfaces. Mater Design. https://doi.org/10.1016/j.matdes.2021.110050
15. Callens S, Arns C, Kuliesh A, Zadpoor A (2021) Decoupling minimal surface metamaterial properties through multi-material hyperbolic tilings. Adv Functional Mater. https://doi.org/10.1002/adfm.202101373
16. Daynes S (2024) Isotropic cellular structure design strategies based on triply periodic minimal surfaces. Addit Manuf 81:104010. https://doi.org/10.1016/j.addma.2024.104010
17. Yin H, Liu Z, Dai J, Wen G, Zhang C (2020) Crushing behavior and optimization of sheet-based 3D periodic cellular structures. Composites Part B: Eng. https://doi.org/10.1016/j.compositesb.2019.107565
18. Almesmari A, Alagha AN, Naji MM, Sheikh-Ahmad J, Jarrar F (2023) Recent advancements in design optimization of lattice-structured materials. Adv Eng Mater. https://doi.org/10.1002/adem.202201780
19. AlQaydi HA, Krishnan K, Oyebanji J, Lee DW, Alneyadi SA, Ghisi N, Kindleyside L, Aboulkhair NT (2022) Hybridisation of AlSi10Mg lattice structures for engineered mechanical performance. Addit Manuf. https://doi.org/10.1016/j.addma.2022.102935
20. Bonatti C, Mohr D (2019) Smooth-shell metamaterials of cubic symmetry: Anisotropic elasticity, yield strength and specific energy absorption. Acta Materialia 164:301–321. https://doi.org/10.1016/j.actamat.2018.10.034
21. Gao T, Liu K, Wang X, Wei K, Wang Z (2024) Multi-level mechanism of biomimetic TPMS hybridizations with tailorable global homogeneity and heterogeneity. Extreme Mech Lett. https://doi.org/10.1016/j.eml.2024.102136
22. Zhang X, Yan S, Xie X, Li Y, Wang C, Wen P (2024) Multi-dimensional hybridized TPMS with high energy absorption capacity. Int J Mech Sci. https://doi.org/10.1016/j.ijmecsci.2024.109244
23. Plocher J, Panesar A (2020) Effect of density and unit cell size grading on the stiffness and energy absorption of short fibre-reinforced functionally graded lattice structures. Addit Manuf. https://doi.org/10.1016/j.addma.2020.101171
24. Ozdemir M, Simsek U, Kiziltas G, Gayir CE, Celik A, Sendur P (2023) A novel design framework for generating functionally graded multi-morphology lattices via hybrid optimization and blending methods. Addit Manuf. https://doi.org/10.1016/j.addma.2023.103560
25. Chen R, Zhang W, Jia Y, Wang S, Cao B, Li C, Du J, Yu S, Wei J (2024) Ultra-stiff and quasi-elastic-isotropic triply periodic minimal surface structures designed by deep learning. Mater Design 244:113107. https://doi.org/10.1016/j.matdes.2024.113107
26. Patel D, Yang R, Wang J, Rai R, Dargush G (2023) Deep learning-based inverse design framework for property targeted novel architectured interpenetrating phase composites. Composite Struct. https://doi.org/10.1016/j.compstruct.2023.116783
27. Wang Y, Zeng Q, Wang J, Li Y, Fang D (2022) Inverse design of shell-based mechanical metamaterial with customized loading curves based on machine learning and genetic algorithm. Comput Methods Appl Mech Eng. https://doi.org/10.1016/j.cma.2022.115571
28. Hu Z, Ding J, Ding S, Ma WWS, Chua JW, Li X, Zhai W, Song X (2024) Machine learning - enabled inverse design of shell-based lattice metamaterials with optimal sound and energy absorption. Virtual PhysPrototyping 19(1):2412198. https://doi.org/10.1080/17452759.2024.2412198
29. Chen Z, Xie YM, Wu X, Wang Z, Li Q, Zhou S (2019) On hybrid cellular materials based on triply periodic minimal surfaces with

extreme mechanical properties. Mater Design 183:108109. https://doi.org/10.1016/j.matdes.2019.108109
30. Pais A, Alves JL, Jorge RN, Belinha J (2023) Multiscale homogenization techniques for TPMS foam material for biomedical structural applications. Bioengineering. https://doi.org/10.3390/bioengineering10050515
31. Gao J, Li H, Gao L, Xiao M (2018) Topological shape optimization of 3D micro-structured materials using energy-based homogenization method. Adv Eng Software 116:89–102. https://doi.org/10.1016/j.advengsoft.2017.12.002
32. Somnic J, Jo B (2022) Status Challenges Homogenization Methods Lattice Mater. Materials 15:605. https://doi.org/10.3390/ma15020605
33. Zhmaylo M, Maslov L, Borovkov A, Tarasenko F (2023) Finite element homogenization and experimental evaluation of additively manufactured lattice metamaterials. J Brazilian Soc Mech Sci Eng. https://doi.org/10.1007/s40430-023-04210-0
34. Zhenze Y, Yu C-H, Guo K, Buehler M (2021) End-to-end deep learning method to predict complete strain and stress tensors for complex hierarchical composite microstructures. J Mech Phys Solids 154:104506. https://doi.org/10.1016/j.jmps.2021.104506
35. Xiaolei C, Dingreville R, Richeton T, Berbenni S (2022) Invariant surface elastic properties in FCC metals and their correlation to bulk properties revealed by machine learning methods. J Mech Phys Solids 163:104852. https://doi.org/10.1016/j.jmps.2022.104852
36. Li X, Liu Z, Cui S, Luo C, Li C-F, Zhuang Z (2019) Predicting the effective mechanical property of heterogeneous materials by image based modeling and deep learning. Comput Methods Appl Mech Eng. https://doi.org/10.1016/j.cma.2019.01.005
37. Yu G, Xiao L, Song W (2022) Deep learning-based heterogeneous strategy for customizing responses of lattice structures. Int J Mech Sci 229:107531. https://doi.org/10.1016/j.ijmecsci.2022.107531
38. Liu C, Li S (2023) High-resolution topology optimization method of multi-morphology lattice structures based on three-dimensional convolutional neural networks (3D-CNN). Struct Multidiscip Optim. https://doi.org/10.1007/s00158-023-03688-5
39. Viet NV, Zaki W (2023) Artificial neural network model of the mechanical behaviour of shape memory alloy Schwartz primitive lattice architectures. Mech Mater. https://doi.org/10.1016/j.mechmat.2023.104680
40. Ibrahimi S, D'Andrea L, Gastaldi D, Rivolta MW, Vena P (2024) Machine learning approaches for the design of biomechanically compatible bone tissue engineering scaffolds. Comput Methods Appl Mech Eng. https://doi.org/10.1016/j.cma.2024.116842
41. Feng J, Fu J, Yao X, He Y (2022) Triply periodic minimal surface (TPMS) porous structures: from multi-scale design, precise additive manufacturing to multidisciplinary applications. Int J Extreme Manuf. https://doi.org/10.1088/2631-7990/ac5be6
42. Paul MJ, Liu Q, Best JP, Li X, Kruzic JJ, Ramamurty U, Gludovatz B (2021) Fracture resistance of AlSi10Mg fabricated by laser powder bed fusion. Acta Materialia 211:116869. https://doi.org/10.1016/j.actamat.2021.116869
43. Singh D, Sharma S, Kumar R, Vaish R (2023) Representative volume element model of triply periodic minimal surfaces (TPMS)-based electrostrictive composites for numerical evaluation of effective properties. Acta Mechanica 234(2):355–375. https://doi.org/10.1007/s00707-022-03404-2
44. Yang Y, Shan M, Zhao L, Qi D, Zhang J (2019) Multiple strut-deformation patterns based analytical elastic modulus of sandwich BCC lattices. Mater Design 181:107916. https://doi.org/10.1016/j.matdes.2019.107916
45. Lu Y, Zhao W, Cui Z, Zhu H, Wu C (2019) The anisotropic elastic behavior of the widely-used triply-periodic minimal surface based scaffolds. J Mech Behav Biomed Mater 99:56–65. https://doi.org/10.1016/j.jmbbm.2019.07.012
46. Chen Y-Z, Wang C-H, Hsieh T-Y, Tung C-C, Chen P-Y, Huang T-H (2024) An efficient parameterized neural network enhanced multiscale finite element modeling for triply periodic minimal surface meta-structures and its applications for femur. J Mater Res Technol 30:6176–6194. https://doi.org/10.1016/j.jmrt.2024.05.023
47. Zener CM, Siegel S (1949) Elasticity and anelasticity of metals. J Phys Colloid Chem. https://doi.org/10.1021/j150474a017
48. Shojaee M, Valizadeh I, Klein DK, Sharifi P, Weeger O (2023) Multiscale modeling of functionally graded shell lattice metamaterials for additive manufacturing. Eng Comput. https://doi.org/10.1007/s00366-023-01906-8
49. Gibson LJ, Ashby MF (1997) The mechanics of foams: basic results. Cambridge solid state science series. Cambridge University Press, Cham, pp 175–234
50. Guo X, Zheng X, Yang Y, Yang X, Yi Y (2019) Mechanical behavior of TPMS-based scaffolds: a comparison between minimal surfaces and their lattice structures. SN Appl Sci. https://doi.org/10.1007/s42452-019-1167-z
51. Sokollu B, Gulcan O, Konukseven EI (2022) Mechanical properties comparison of strut-based and triply periodic minimal surface lattice structures produced by electron beam melting. Addit Manuf 60:103199. https://doi.org/10.1016/j.addma.2022.103199
52. Maconachie T, Tino R, Lozanovski B, Watson M, Jones A, Pandelidi C, Alghamdi A, Almalki A, Downing D, Brandt M, Leary M (2020) The compressive behaviour of ABS gyroid lattice structures manufactured by fused deposition modelling. Int J Adv Manuf Technol 107:11–12. https://doi.org/10.1007/s00170-020-05239-4
53. Chen Z, Wu B, Chen X, Xie YM (2023) Energy absorption and impact resistance of hybrid triply periodic minimal surface (TPMS) sheet-based structures. Mater Today Commun 37:107352. https://doi.org/10.1016/j.mtcomm.2023.107352